Eurasian Journal of Physics and Functional Materials

Manuscript 1190

Utilizing TiO2 nanostructures to synthesize plate-like Bi4Ti3O12 templates via molten salt method

Le Tran Uyen Tu

Le Dai Vuong

ORIGINAL STUDY

Utilizing TiO_2 Nanostructures to Synthesize Plate-like $Bi_4Ti_3O_{12}$ Templates Via Molten Salt Method

Le T. Uyen Tu [a], Le D. Vuong [b,*]

[a] University of Sciences, Hue University, Vietnam
[b] School of Engineering and Technology, Hue University, Vietnam

Abstract

Plate-like $Bi_4Ti_3O_{12}$ templates were synthesized through the molten salt method using TiO_2 nanostructures. The effect of sintering temperature on the structure, morphologies, and dielectric properties of $Bi_4Ti_3O_{12}$ templates was investigated. Experimental results showed that the single-phase $Bi_4Ti_3O_{12}$ templates were successfully obtained within a temperature range of 950−1050 °C. With increasing sintering temperature, the plate-like $Bi_4Ti_3O_{12}$ templates were formed with the average length of the particles increasing and reaching a maximum value of 9.5 μm at 1050 °C before decreasing. The grain size followed a gradual spreading mechanism, where the $Bi_4Ti_3O_{12}$ nuclei diffused to the growth steps, forming larger plate-like particles and eventually $Bi_4Ti_3O_{12}$ templates. In addition, $Bi_4Ti_3O_{12}$ templates sintered at 1050 °C demonstrated superior performance, with a high dielectric constant of 595 and low dielectric loss of 0.042 compared to the other samples. This performance aligns with their degree of orientation, relative density, and grain size development. Experimental findings further revealed that $Bi_4Ti_3O_{12}$ possesses potential for ferroelectric properties, with a remanent polarization of 6.9 μC/cm^2. These results provide valuable insights for selecting orientation templates to fabricate textured ceramics.

Keywords: Nanotechnology, $Bi_4Ti_3O_{12}$ templates, Degree of orientation, TiO_2 nanostructures, Molten salt method

1. Introduction

Bismuth titanate ($Bi_4Ti_3O_{12}$) was first found by Aurivillius [1] in 1949. The general formula for the Aurivillius phase is $A_{m-1}Bi_2B_mO_{3m+3}$. The structure consists of the alternating layers of pseudoperovskite blocks with the composition $(A_{m-1}B_mO_{3m+1})^{2-}$ and fluorite-like bismuth oxygen layers with the composition $(Bi_2O_2)^{2+}$, where A represents a mono-, di-, or trivalent cation, B signifies cations with valencies of 3, 4, or 5, and m denotes the number of perovskite layers. In $Bi_4Ti_3O_{12}$, m = 3, A = Bi^{3+}, and B = Ti^{4+} [2]. $Bi_4Ti_3O_{12}$ is one of the simplest bismuth titanate compounds, characterized by a perovskite structure composed of alternating layers of Bi_2O_3 and TiO_2 [3]. Due to its excellent dielectric, ferroelectric, and piezoelectric properties, $Bi_4Ti_3O_{12}$ is widely applied to sensors and memory devices [4]. In addition, with a ferroelectric to paraelectric phase transition temperature of 675 °C, $Bi_4Ti_3O_{12}$ is a potential candidate for high-temperature piezoelectric devices [5]. In recent years, considerable efforts have been devoted in finding the optimal fabrication method of $Bi_4Ti_3O_{12}$ at low calcination temperatures [6], and the most common synthesis routes include chemical coprecipitation method [7] (precipitation [8] and the modified oxalate co-precipitation method [9]), sol-gel [10,11], hydrothermal [12,13], urea method [14], citrate method [15], high-energy milling [16,17], polymeric precursor method [17], molten salt method [18], and solid phase method [18]. $Bi_4Ti_3O_{12}$ generally possesses a typical anisotropic plate-like microstructure with a low coercive field (*Ec*), a small remanent polarization (*Ps*), excellent fatigue properties, and remarkable retention time. However, there have been no reports on the synthesis of $Bi_4Ti_3O_{12}$ templates using TiO_2 nanostructures.

In our recent study, we presented the synthesis of TiO_2 nanostructures via an ultrasound-assisted method

Received 2 April 2024; revised 21 May 2024; accepted 28 May 2024.
Available online 20 July 2024

* Corresponding author.
E-mail address: ldvuong@hueuni.edu.vn (L.D. Vuong).

https://doi.org/10.69912/2616-8537.1190

employing commercially available TiO_2 particles and sulfuric acid [19]. This method is highly reproducible and stable, offering a viable approach for synthesizing TiO_2 nanoparticles suitable for synthesizing $Bi_4Ti_3O_{12}$ templates and other electrical materials containing Ti, such as $Bi_{0.5}Na_{0.5}TiO_3$ and $Bi_{0.5}K_{0.5}TiO_3$ ceramics. Meanwhile, recent research findings indicate that the use of TiO_2 nanoparticles leads to a reduction in sintering temperature while enhancing desired properties. In this direction, Pavlov et al. [20] suggested that the properties of beryllium ceramics were modified through the incorporation of TiO_2 nanoparticles. Similarly, Han et al. [21] successfully synthesized a $BaTiO_3$ ceramic system utilizing TiO_2 nanoparticles. Additionally, Chuong et al. [22] revealed that TiO_2 nanotubes significantly decreased the sintering temperature and improved the density and piezoelectric properties of the PZT ceramics. Thus, using nanostructured materials as starting materials enables the formation of $Bi_4Ti_3O_{12}$ with high electrical properties at lower sintering temperatures.

In this study, $Bi_4Ti_3O_{12}$ templates were synthesized through the molten salt method using TiO_2 nanostructures. This work aims to synthesize $Bi_4Ti_3O_{12}$ templates intended for future application in the fabrication of oriented Bi-based ceramics. Besides, this method is an exciting addition to the large repertoire of $Bi_4Ti_3O_{12}$ template synthesis techniques and facilitates the characterization of the fabricated $Bi_4Ti_3O_{12}$ templates.

2. Materials and methodology

2.1. Synthesis of $Bi_4Ti_3O_{12}$ templates

In this study, the $Bi_4Ti_3O_{12}$ was prepared using Bi_2O_3 and TiO_2 nanoparticles. Firstly, TiO_2 nanoparticles in an anatase crystal were synthesized via an ultrasound-assisted method using commercial TiO_2 particles and sulfuric acid [19]. Structural analysis of the TiO_2 through X-ray diffraction (XRD) patterns and Raman spectroscopy confirmed the presence of pure anatase, as shown in Fig. 1(a). The obtained TiO_2 nanoparticles are spherical, with an average size ranging from 4 nm to 35 nm, as depicted in Fig. 1(b).

Secondly, Bi_2O_3 and TiO_2 were weighed and milled in ethanol under ultrasound (with an electric power of 100 W and a fixed frequency of 28 kHz) for 1 h. After drying, the powder was calcined at 500 °C for 2 h to obtain the $Bi_4Ti_3O_{12}$ precursor. It is reported that a liquid phase typically forms in a Bi_2O_3-rich $Bi_4Ti_3O_{12}$ structure at 865–870 °C, signifying that $Bi_4Ti_3O_{12}$ must be sintered at temperatures above 870 °C. Finally, the amorphous $Bi_4Ti_3O_{12}$ powder and the Na_2CO_3/K_2CO_3 eutectic mixture were mixed in a sealed alumina crucible and sintered at 950 °C, 1000 °C, 1050 °C, and 1100 °C for 2 h. The reaction of $Bi_4Ti_3O_{12}$ synthesis can be depicted as follows:

$$2Bi_2O_3 + 3TiO_2 \rightarrow Bi_4Ti_3O_{12} + \frac{1}{2}O_2 \quad (1)$$

2.2. Characterization of the materials

The crystalline phase of the sintered ceramics was examined by X-ray diffraction (XRD, D8 Advance) under Cu-K_α radiation at a wavelength of 1.5405 Å, in the 2θ range of 20°–70°, and with a step size of 0.02°, at room temperature (*RT*). Surface morphologies were examined by field-emission scanning electron microscopy (FESEM; Nova NanoSEM 450-FEI-HUS-VNU), and sample densities were measured by the Archimedes method. Raman scattering spectra were recorded from a Raman Spectrometer (Jobin-Yvon Inc., Paris, France) using a backscattering configuration; the excitation laser was irradiated from an Ar^+ laser with a wavelength of 488 nm and output power of 11 mW. Energy dispersive spectra (EDS) were measured using a Hitachi S-3400 N scanning electron microscope with an EDS system Thermo Noran. The Lotgering method was

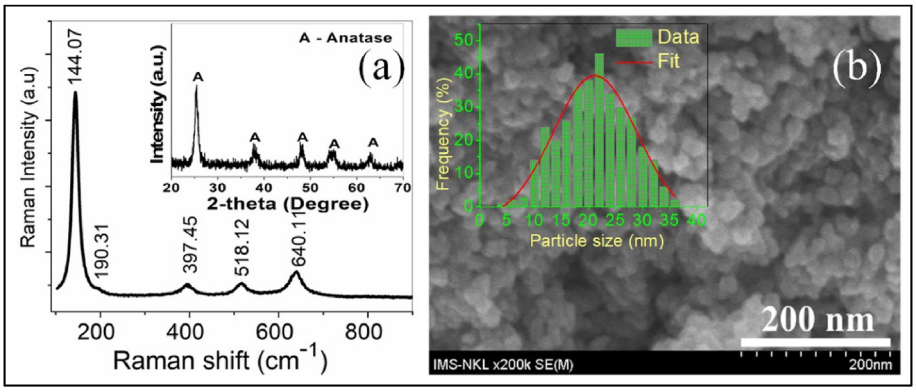

Fig. 1. (a) Structure and, (b) Microstructure characteristics of TiO_2 nanoparticles.

employed to evaluate the degree of orientation, and grain size was determined by the mean linear intercept method. Dielectric properties were obtained using an LCR meter by measuring the capacitance and loss at room temperature (RT) and at 500 °C.

3. Results and discussion

Raman spectroscopy was utilized to characterize the obtained TiO_2 nanoparticles, confirming the phase purity of the anatase TiO_2 [23], as shown in Fig. 1(a). Anatase TiO_2 nanoparticles were formed after annealing at 550 °C. The Raman spectrum displayed five prominent peaks at 146.45 cm^{-1} (E_g), 190.31 cm^{-1} (E_g), 394.99 cm^{-1} (B_{1g}), 514.51 cm^{-1} (A_{1g}), and 635.55 cm^{-1} (E_g), indicating the presence of anatase TiO_2 phase, in accordance with the XRD results mentioned above (Insert Fig. 1(a)). Furthermore, the peaks observed at 2θ values of 25.28°, 37.78°, 48.05°, 55.01°, and 62.61° correspond to the reflections from the (101), (004), (200), (211), and (204) lattice planes of anatase TiO_2 [19,24]. Besides, the scanning electron microscopy (SEM) images (Fig. 1(b)) reveal TiO_2 nanoparticles with a spherical shape, showcasing an average size of 5–35 nm (Insert Fig. 1(b)). The particle size distribution was determined using data obtained from SEM images processed through ImageJ software, which were then fitted into a Gaussian distribution plot [25].

Fig. 2 presents the major findings of the XRD analysis of $Bi_4Ti_3O_{12}$ templates within the 2θ range of 10–70°. The as-synthesized $Bi_4Ti_3O_{12}$ templates mainly exhibited an orthorhombic perovskite structure, with no other impurities observed in the temperature range of 950–1050 °C. The presence of the orthorhombic perovskite structure was further confirmed by the Rietveld refinement of XRD data for all the $Bi_4Ti_3O_{12}$ templates sintered at different temperatures, as displayed in Fig. 2.

The crystal structure parameters for $Bi_4Ti_3O_{12}$ in the space group *Fmmm* were calculated from the Rietveld refinement, which were compared with reported values of $Bi_4Ti_3O_{12}$ crystal [18,26]. The fitting analysis, including peak shape, peak position, structure, and background, was performed in terms of profile-refined parameters, as summarized in Table 1.

Furthermore, the intensity of the (006), (008), and (0014) peaks, corresponding to the *a*–*b* plane perpendicular to the *c*-axis of the $Bi_4Ti_3O_{12}$ sample, exhibited a notable variation trend. Specifically, their intensities increased and reached their peak at 1050 °C before decreasing. Additionally, the intensity of the (00*l*) diffraction peak gradually decreased at 1100 °C due to the formation of the $Bi_2Ti_2O_7$ (pyrochlore

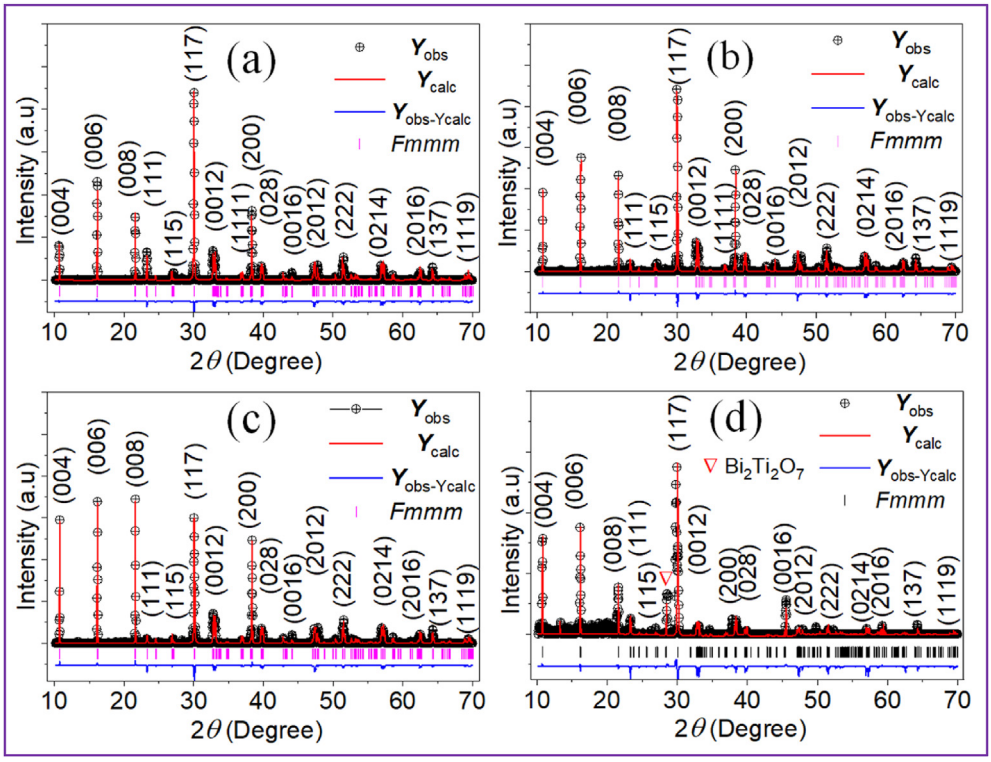

Fig. 2. Rietveld refined XRD patterns of $Bi_4Ti_3O_{12}$ templates sintered at different temperatures for 2 h: (a) 950 °C, (b) 1000 °C, (c) 1050 °C, and (d) 1100 °C.

Table 1. Crystal structure parameters of $Bi_4Ti_3O_{12}$ samples calculated by the Rietveld refinement of XRD patterns.

Sintering temperature	a (Å)	b (Å)	c (Å)	V (Å^3)	R_{wp} (%)	R_p (%)	χ^2
950 °C	5.4124	5.4485	32.829	968.11	7.6	6.2	2.37
1000 °C	5.4099	5.4479	32.839	967.85	7.2	5.9	2.22
1050 °C	5.4096	5.4480	32.839	967.82	6.9	5.7	2.19
1100 °C	5.4094	5.4487	32.838	967.87	8.4	6.6	3.15

phase). This variation in densification behavior during sintering can be attributed to defect chemistry and the creation of oxygen vacancies [27]. In other words, the synthesis of $Bi_4Ti_3O_{12}$ materials at high temperatures leads to the evaporation of Bi, potentially resulting in the formation of non-stoichiometric structural defects in the $Bi_2Ti_2O_7$ [28]. Therefore, it was necessary to consider the presence of excess Bi_2O_3 to account for its volatility during the calcination process, ensuring that the stoichiometry of the $Bi_4Ti_3O_{12}$ templates is maintained. As noted by Andrew et al. [29], pyrochlore-type bismuth titanate (space group = $Fd\ \bar{3}\ m$, with a = 10.37949 Å) exists as a minor phase alongside $Bi_2Ti_4O_{11}$ and $Bi_4Ti_3O_{12}$. Meanwhile, Čontala et al. [30] suggested that during the preparation of $Bi_4Ti_3O_{12}$ from Bi_2O_3 and TiO_2 through the molten salt method or solid-state reaction, secondary phases such as $Bi_{12}TiO_{20}$ or $Bi_2Ti_2O_7$ are commonly formed, and must be removed to enhance the electrical properties of $Bi_4Ti_3O_{12}$. In our experiment, the appearance of the $Bi_2Ti_2O_7$ at 1100 °C can be attributed to the loss of Bi in the mixture, resulting from Bi-vapor evaporation at high temperatures [31]. Consequently, a Ti-rich $Bi_2Ti_2O_7$ crystalline phase was formed [32]. Kargin et al. [33] showed that $Bi_2Ti_2O_7$ generally emerges between 1000 °C and 1210 °C. Moreover, it was found that the pyrochlore phase was not completely stoichiometric due to the formation of cation-deficient samples at high temperatures.

The total shrinkage after sintering was calculated using Eq. (2).

$$\text{Shrinkage ratio} = \frac{|d_b - d_a|}{d_a}.100\% \quad (2)$$

where d_b and d_a represent the diameters of the sample before and after sintering, respectively.

It is evident from Fig. 3 that the shrinkage ratio was profoundly dependent on the sintering temperature. It is observed that the shrinkage ratio gradually increased with rising sintering temperature until 1050 °C, after which it decreased slightly. Further, the sample density exhibited an increase from 6.29 g/cm^3 to 7.91 g/cm^3 with the increasing sintering temperature from 950 °C to 1100 °C, followed by a significant decrease. The theoretical density was calculated using Eq. (3).

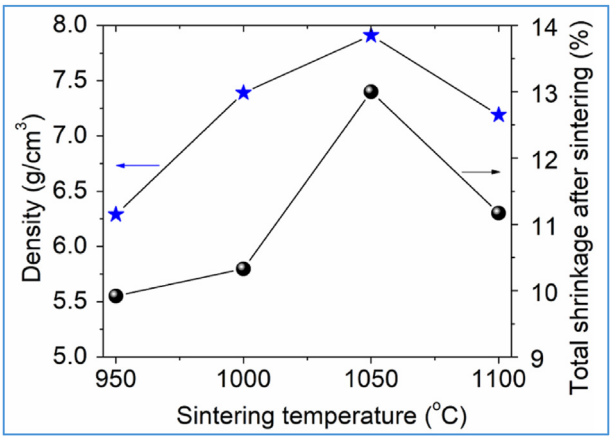

Fig. 3. Density and total shrinkage after sintering of $Bi_4Ti_3O_{12}$ templates at different temperatures.

$$\rho = \frac{(number\ of\ atoms/unit\ cell)(atomic\ mass)}{(volume\ of\ unit\ cell)(Avogadro's\ Number)} \quad (3)$$

The theoretical density of 8.04 g/cm^3 was employed to calculate the relative density. The relative density increased from 78.23% to 98.38% as the sintering temperature rose from 950 °C to 1100 °C, reaching its highest value of 98.38% at 1050 °C (corresponding to a density of 7.91 g/cm^3, see Fig. 3). The degree of orientation of $Bi_4Ti_3O_{12}$ templates was determined based on the Lotgering orientation factor (LOF; f) [34] using the XRD data recorded across a 2θ range of 10°–60°.

$$f = \frac{P - P_o}{1 - P_o} \quad (4)$$

where $P = \frac{\sum I(00l)}{\sum I(hkl)}$, $P_o = \frac{\sum I(00l)}{\sum I(hkl)}$, $\sum I(00l)$ and $\sum I(hkl)$ are, respectively, the sums of the intensities of $(00l)$ and (hkl) reflections, and P_o is the value of P for the sintered $Bi_4Ti_3O_{12}$ templates. The values of (f) for the $Bi_4Ti_3O_{12}$ template sintered at 950 °C, 1000 °C, 1050 °C, and 1100 °C for 2 h were measured as 0.42, 0.54, 0.71, and 0.56 respectively (Fig. 4). In addition, it is discernible from Fig. 4 that the degree of orientation increased with the rising sintering temperature, reaching its peak value (f = 0.71) at 1050 °C. Patwardhan et al. [35] reported values of f for a calcined

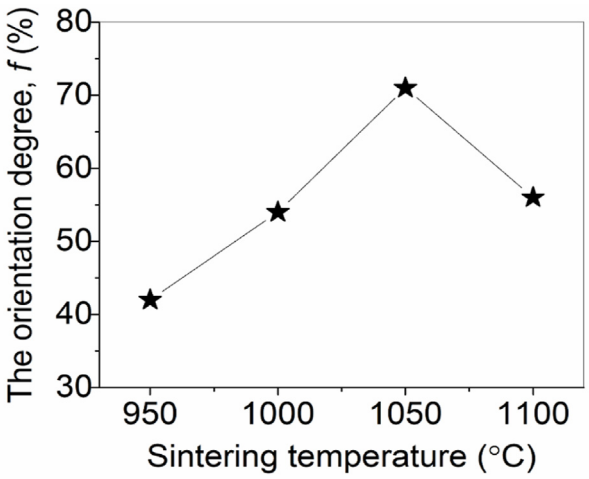

Fig. 4. Lotgering factor for $Bi_4Ti_3O_{12}$ templates as a function of temperature.

$Bi_4Ti_3O_{12}$ powder sample ranging from 0.20 to 0.30; however, $Bi_4Ti_3O_{12}$ powder hot forged for 75 min at 1050 °C under a pressure of 5 MPa manifested a high degree of orientation ($f = 0.97$). Xiang et al. [36] successfully fabricated *c*-axis-oriented $Bi_4Ti_3O_{12}$ thick films with $f = 0.98$ through templated grain growth technique. Conversely, Kimura et al. [37] prepared *c*-axis-oriented $Bi_4Ti_3O_{12}$ structures with $f = 0.89$ using the traditional solid-state reaction method. This suggests that the rearrangement process plays a key role in the early stages of the sintering process. As the rearrangement progresses, diffusional mass transport becomes the prevailing phenomenon [35]. However, at high sintering temperatures, stronger grain vibrations cause the partial return of the orientation, resulting in a higher degree of orientation with increasing relative density.

Fig. 5 displays the morphologies of $Bi_4Ti_3O_{12}$ templates sintered at various temperatures for 2 h. The fabrication temperature yielded profound effects on both the growth rate and crystallization of $Bi_4Ti_3O_{12}$. As the sintering temperature increased, the length of the $Bi_4Ti_3O_{12}$ templates gradually increased, and their shapes changed from lumpy to plate-like structures, which is a main characteristic of $Bi_4Ti_3O_{12}$ [38]. ImageJ software was used to assess the influence of sintering temperature on the size development of the templates. Fig. 6 shows the length distribution of the $Bi_4Ti_3O_{12}$ templates sintered at 950 °C, 1000 °C, 1050 °C, and 1100 °C. It is apparent that the sintering temperature strongly influenced the microstructure of the $Bi_4Ti_3O_{12}$ templates. The length of the $Bi_4Ti_3O_{12}$ particles increased with rising sintering temperature, reaching its maximum value of 9.5 μm at 1050 °C with their shapes changed from lumpy to a plate-like structure. This

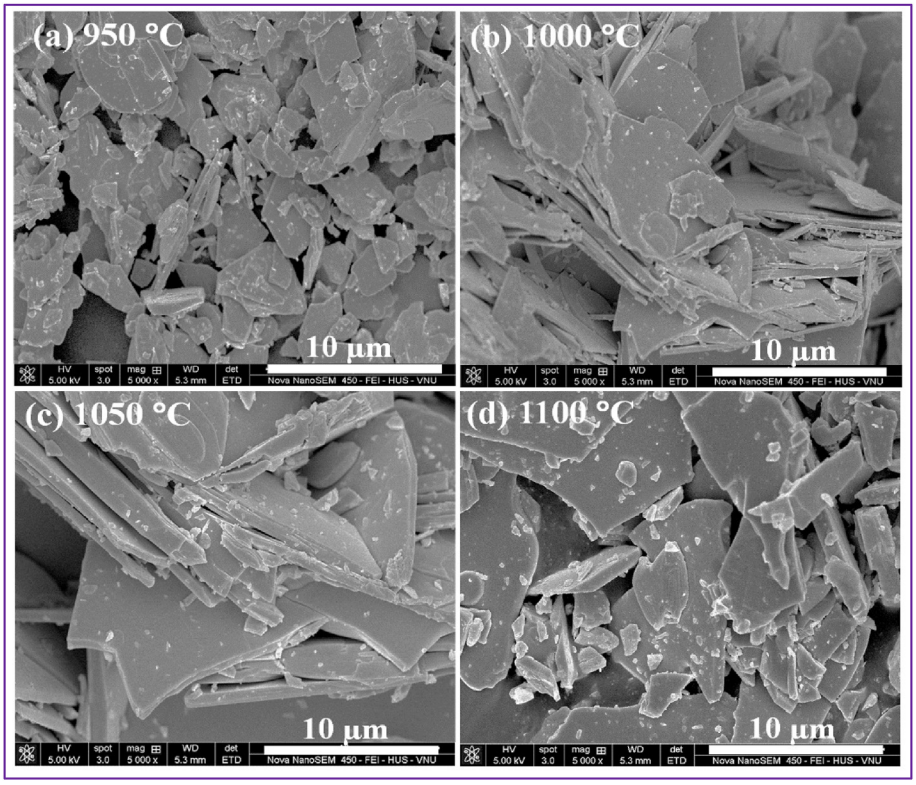

Fig. 5. The morphology and arrangement of particles of the $Bi_4Ti_3O_{12}$.

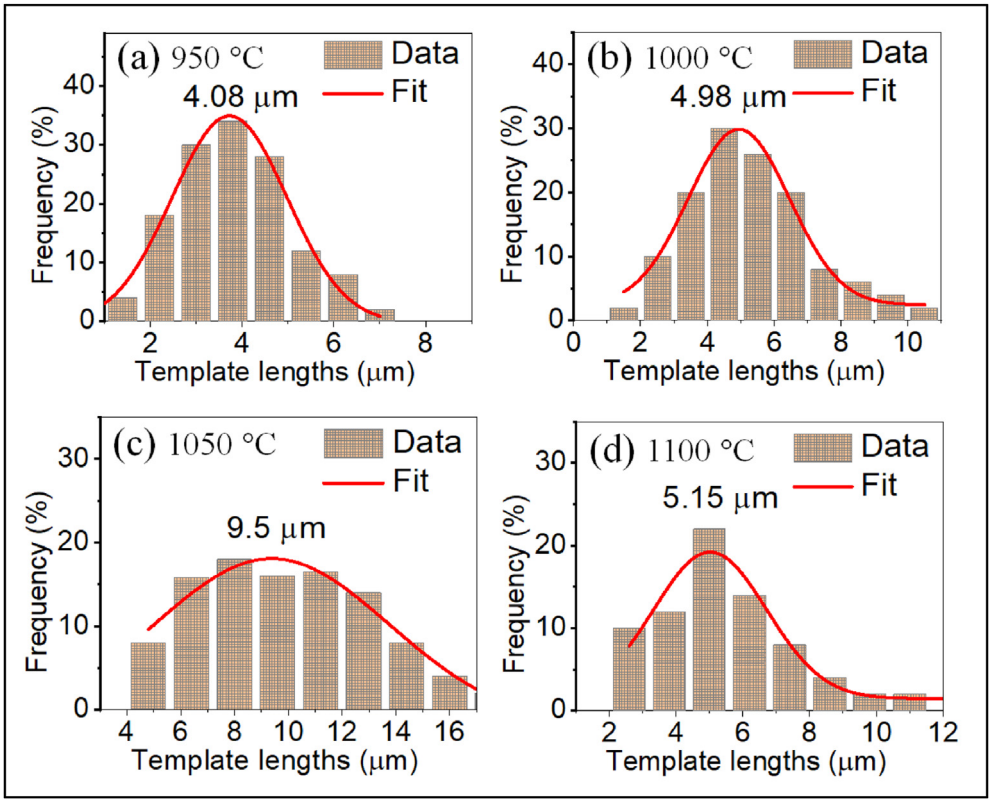

Fig. 6. The length distribution of the $Bi_4Ti_3O_{12}$ templates at different heating temperatures.

observation is consistent with the ceramic density results depicted in Fig. 3. This observation is in agreement with the findings reported by Ref. [38]. The evolution of particle size can be explained through the formation mechanism of $Bi_4Ti_3O_{12}$ templates, as represented in Fig. 7. In the molten salt method, particle formation occurs in two stages: reaction and growth. During the reaction stage, reactant particles dissolve into the molten salt to generate product particles [37]. As noted by Ranieria et al. [38], particle size undergoes rapid increase during the formation process, with the growth rate of each crystal face dictating the outer shape of the particles. Furthermore, as particle size increases slowly during the growth process, the primary surface

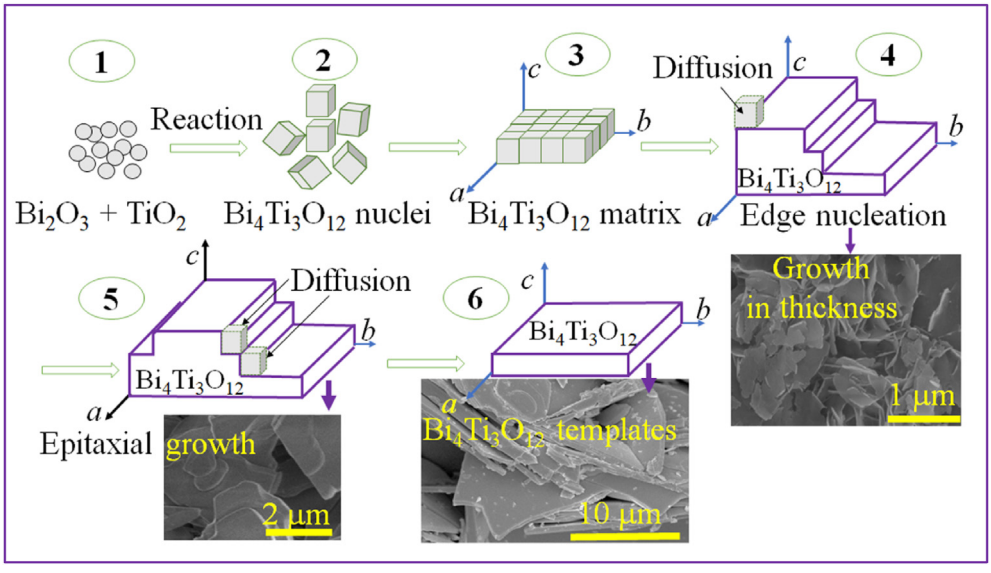

Fig. 7. Formation mechanism of $Bi_4Ti_3O_{12}$ templates.

becomes dominated by facets with minimum interfacial energy. Kimura et al. [37] suggest that $Bi_4Ti_3O_{12}$ forms when two reactants exhibit comparable dissolution rates in molten salt. Therefore, at the initial stage of the reaction, lumpy $Bi_4Ti_3O_{12}$ powders were formed depending on the degree of interaction between $Bi_4Ti_3O_{12}$ and molten salt. Subsequently, more plate-like particles were formed as the $Bi_4Ti_3O_{12}$ crystal started to grow along the (00*l*) plane with increasing sintering temperature [39]. Additionally, dimensional crystal nuclei were formed at the edge of the $Bi_4Ti_3O_{12}$ matrix, thereby increasing the thickness of the product layer.

The formation mechanism of $Bi_4Ti_3O_{12}$ templates is illustrated in Fig. 7. Initially, $Bi_4Ti_3O_{12}$ nuclei (stage 2) were obtained through a solid-state reaction between Bi_2O_3 and TiO_2 (stage 1). These nuclei then aggregated and rearranged to form a plate-like $Bi_4Ti_3O_{12}$ matrix (stage 3). Subsequently, the $Bi_4Ti_3O_{12}$ nuclei diffused to the growth steps (stage 4), resulting in the formation of larger plate-like particles (stage 5) and, ultimately, $Bi_4Ti_3O_{12}$ templates (stage 6).

Fig. 8(a) presents the energy-dispersive X-ray spectroscopy (EDS) analysis of $Bi_4Ti_3O_{12}$ templates sintered at 1050 °C for 2 h. The energy values of the characteristic X-rays for the elements were measured as follows: 2.42 keV, 10.82 keV, and 13.02 keV for Bi, 4.51 keV and 4.97 keV for Ti, and 0.53 keV for O. These results are consistent with those reported by Chen et al. [26]. According to author Liang et al. [40], the crystal structure of $Bi_4Ti_3O_{12}$ consists of perovskite layers and bismuth oxygen layers, they are periodically arranged along the *c*-axis direction observed in Fig. 8(b). As mentioned above, the general formula of the Aurivillius phase is $A_{m-1}Bi_2B_mO_{3m+3}$, and it consists of the alternating layers of pseudo perovskite blocks of composition $(A_{m-1}B_mO_{3m+1})^{2-}$ and fluorite-like bismuth oxygen layers of composition $(Bi_2O_2)^{2+}$, where the integer, *m*, describes the number of sheets of corner-sharing BO_6 octahedra forming the ABO_3 perovskite blocks. Furthermore, it is supported by the results of the Raman spectroscopy, as shown in Fig. 9. The Raman modes located at 109, 264, 444, 534, and 850 cm^{-1} are indicative of the $Bi_4Ti_3O_{12}$ template [41]. Specifically, the appearance of a Raman mode at a low frequency (109 cm^{-1}) is due to the atomic mass of Bi ions, leading to Bi displacements in the Bi_2O_2 layer, and is assigned to vibrations between Bi and O atoms [41]. Additionally, the Raman modes at 264, 444, and 534 cm^{-1} can be attributed to the internal mode of the TiO_6 octahedron, while the peak at 850 cm^{-1} is ascribed to the symmetric Ti–O stretching vibration [42].

Besides, to study the effects of frequency and temperature measured on the dielectric properties of the $Bi_4Ti_3O_{12}$ at different heating temperatures, the dielectric constant (ϵ_r) and dielectric loss (tanδ) were measured at 100 kHz and room temperature, as well as at 10 kHz and 500 °C. The corresponding values are presented in Table 2. As indicated in Table 2, the

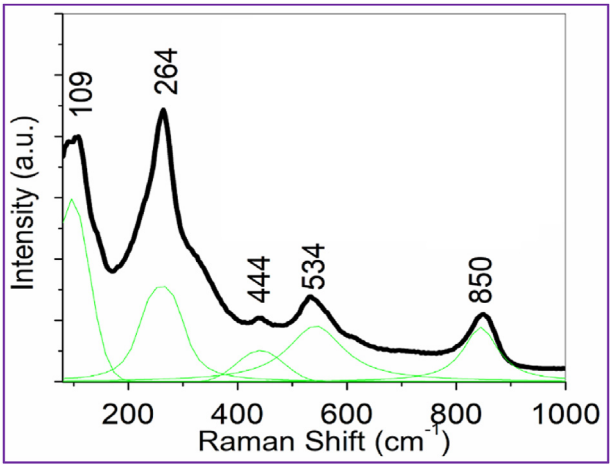

Fig. 9. EDS spectrum of $Bi_4Ti_3O_{12}$ templates sintered at 1050 °C for 2 h.

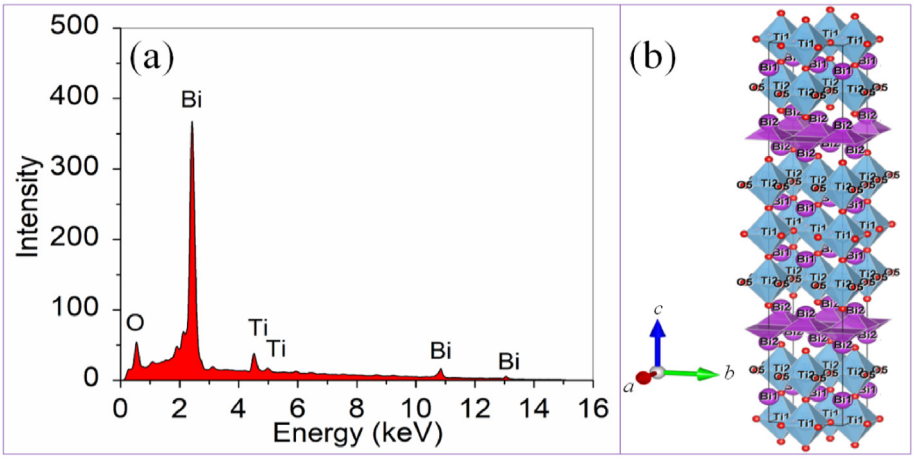

Fig. 8. (a) EDS spectrum of $Bi_4Ti_3O_{12}$ templates sintered at 1050 °C; (b) Schematic diagram of their ABO_3 perovskite blocks.

Table 2. Dielectric parameters of $Bi_4Ti_3O_{12}$ templates at different temperatures and frequencies.

Dielectric parameters	Different heating temperatures $Bi_4Ti_3O_{12}$ templates			
	950 °C	1000 °C	1050 °C	1100 °C
ε_r (100 kHz, RT)	92	102	132	113
Tanδ (100 kHz, RT)	0.092	0.063	0.042	0.051
ε_r (10 kHz, 500 °C)	446	514	595	524
Tanδ (10 kHz, 500 °C)	3.924	2.424	1.924	2.32

$Bi_4Ti_3O_{12}$ templates sintered at 1050 °C demonstrate superior performance, exhibiting a high dielectric constant of 595 and low dielectric loss of 0.042 compared to the other samples. This suggests that the $Bi_4Ti_3O_{12}$ templates sintered at 1050 °C exhibit a notable advantage in orientation, with crystal orientation in ceramics reaching approximately 71% (Fig. 4). This is accompanied by a contribution of 90 domains larger than those observed in other samples. In other words, the presence of well-defined microstructure, minimal grain boundaries, and high ceramic density facilitates the process of polarization rotation. Moreover, the dielectric parameters of the $Bi_4Ti_3O_{12}$ template tend to increase the dielectric constant at 10 kHz and 500 °C. This increase can be attributed to the involvement of oxygen defects contributing to the overall rise in dipoles, thereby facilitating rotation in high-temperature environments, as reported in an earlier study [40].

The aforementioned findings show that the $Bi_4Ti_3O_{12}$ sample sintered at 1050 °C exhibits the most favorable dielectric properties. Consequently, this sample was selected to investigate ferroelectric properties. Fig. 10 depicts the shapes of *P-E* ferroelectric hysteresis loops measured at room temperature for the $Bi_4Ti_3O_{12}$ samples, from which the P_r and E_C were determined. The values of P_r and E_C were observed to be 6.9 μC/cm^2 and 28.7 kV/cm, respectively. These results are in good agreement with previous studies conducted by Liang et al. [40] and Jiang et al. [43] on the ferroelectric properties of $Bi_4Ti_3O_{12}$ materials.

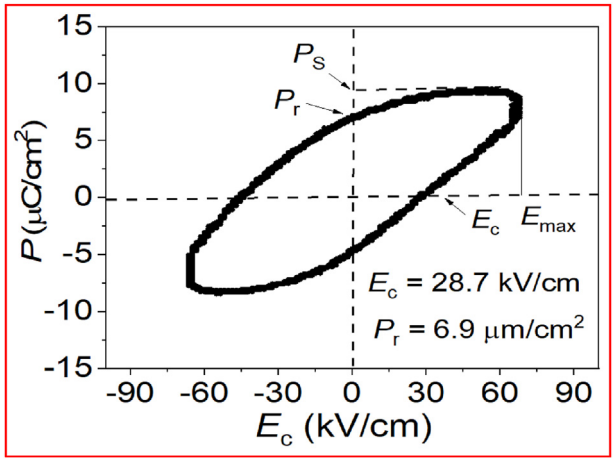

Fig. 10. Ferroelectric propery of $Bi_4Ti_3O_{12}$ sample sintered at 1050 °C.

4. Conclusion

In this study, we successfully utilized nanostructured TiO_2 particles as starting materials to synthesize plate-like $Bi_4Ti_3O_{12}$ templates via a molten salt method. This approach not only allows for low sintering temperatures but also yields high dielectric parameters. Moreover, it proves to be a simple and effective synthesis method, offering control over the morphology and grain size of the templates. As the sintering temperature increased, the formation of plate-like $Bi_4Ti_3O_{12}$ templates occurred, with the average length of the particles increasing and reaching a maximum value of 9.5 μm at 1050 °C, followed by a decrease. Large plate-like $Bi_4Ti_3O_{12}$ templates achieved a grain orientation degree of 71% at 1050 °C. At this temperature, the sample exhibited superior performance, characterized by a high dielectric constant of 595 and low dielectric loss of 0.042, compared to other samples. These outcomes highlight $Bi_4Ti_3O_{12}$ ceramics as promising dielectrics materials suitable for serving as orientation templates in the development of future-oriented ceramic materials.

Conflict of interest

The authors declare that they have no conflict of interest.

Acknowledgments

This research was funded by Ministry of Education and Training under grant number B2023-DHH-30 and Hue University under the Core Research Program, Grant No. NCTB.DHH.2024.08.

References

[1] B. Aurivillius, Ark. Kemi 1 (1949) 499.
[2] J. Wu, N. Qin, E. Lin, B. Yuan, Z. Kang, D. Bao, Nanoscale 11 (2019) 21128–21136.
[3] L. Wang, W. Ma, Y. Fang, Y. Zhang, M. Jia, R. Li, Y. Huang, Proc. Environ. Sci. 18 (2013) 547–558.
[4] W. Wang, K. Zheng, S. Sun, L. Qin, L. Tang, Z. Li, Ceram. Int. 47 (2021) 23518–23527.
[5] F.-C. Sun, S.P. Alpay, S.K. Nayak, Phys. Rev. B 99 (2019) 014101.

[6] H. Zhang, Y. Liang, Y. Zhu, S. Liu, K. Li, J. Yang, W. Lei, J. Alloys Compd. 767 (2018) 1030—1040.
[7] P. Pookmanee, P. Boonphayak, S. Phanichphant, Ceram. Int. 30 (2004) 1917—1919.
[8] S.H. Ng, J. Xue, J. Wang, J. Am. Ceram. Soc. 85 (2002) 2660—2665.
[9] P. Pookmanee, S. Phanichphant, J. Ceram. Process. Res. 10 (2009) 448—452.
[10] A. Rao, A. Robin, S. Kommarneni, J. Cryst. Growth 237 (2002) 469.
[11] F. Yan, G. Zhao, N. Zhao, N. Song, Y. Chen, J. Sol. Gel Sci. Technol. 64 (2012) 524—529.
[12] H. Xu, K.J. Bowman, E.B. Slamovich, J. Am. Ceram. Soc. 86 (2003) 1815—1817.
[13] Z. Zhang, X. Li, Z. Huang, L. Zhang, J. Han, X. Zhou, D. Guo, Y. Ju, J. Mater. Sci. Mater. Electron. 29 (2018) 7453—7457.
[14] M. Anilkumar, S. Dhage, V. Ravi, Mater. Lett. 59 (2005) 514—516.
[15] S. Dhage, Y. Khollam, S. Dhespande, H. Potdar, V. Ravi, Mater. Res. Bull. 39 (2004) 1993—1998.
[16] V. Berbenni, C. Milanese, G. Bruni, A. Girella, A. Marini, J. Therm. Anal. Calorim. 126 (2016) 1507—1511.
[17] B. Stojanovic, A. Simoes, C. Paiva-Santos, C. Quinelato, E. Longo, E. Varela, J. Arana, Ceram. Int. 32 (2006) 707—712.
[18] Z. Xie, X. Tang, J. Shi, Y. Wang, G. Yuan, J.-M. Liu, Nano Energy 98 (2022) 107247.
[19] D.N. Trung, V.L. Dai, S.N. Manh, V.T. Ho, V.C. Truong, Nanomater. Energy 6 (2017) 82—88.
[20] A. Pavlov, Z. Sagdoldina, A. Zhilkashinova, N. Magazov, Z. Turar, S. Gert, Synthesis and investigation of properties of beryllium ceramics modified with titanium dioxide nanoparticles, Materials 16 (2023).
[21] J.-M. Han, M.-R. Joung, J.-S. Kim, Y.-S. Lee, S. Nahm, Y.-K. Choi, J.-H. Paik, J. Am. Ceram. Soc. 97 (2014) 346—349.
[22] Q.T. Dung Le, V.C. Truong, P.A. Do, Adv. Nat. Sci. Nanosci. Nanotechnol. 2 (2011) 025013.
[23] A. Rana, S. Pathak, K. Kumar, A. Kumari, S. Chopra, M. Kumar, D. Kamil, R. Srivastava, S.-K. Kim, R. Verma, S.N. Sharma, Mater. Adv. 5 (2024) 2767—2784.
[24] S. Mahshid, M. Askari, M.S. Ghamsari, J. Mater. Process. Technol. 189 (2007) 296—300.
[25] L.D. Vuong, P.D. Gio, N.D.V. Quang, T. Dai Hieu, T.P. Nam, J. Electron. Mater. 47 (2018) 5944—5951.
[26] Z. Chen, H. Jiang, W. Jin, C. Shi, Appl. Catal. B Environ. 180 (2016) 698—706.
[27] D.V. Le, A.Q. Dao, J. Electroceram. 44 (2020) 68—77.
[28] N. Truong-Tho, L.D. Vuong, J Adv. Dielect. 10 (2020) 2050011.
[29] Hector, A.L. Wiggin, B. Seth, J. Solid State Chem. 177 (2004) 139—145.
[30] A. Čontala, M.M. Kržmanc, D. Suvorov, Acta Chim. Slov. 65 (2018) 630—637.
[31] L. Vuong, N. Truong-Tho, J. Electron. Mater. 46 (2017).
[32] H. Shi, H. Tan, W.-b. Zhu, Z. Sun, Y. Ma, E. Wang, J. Mater. Chem. A 3 (2015) 6586—6591.
[33] Y.F. Kargin, S. Ivicheva, V. Volkov, Russ. J. Inorg. Chem. 60 (2015) 619—625.
[34] F. Lotgering, J. Inorg. Nucl. Chem. 9 (1959) 113—123.
[35] J.S. Patwardhan, M. Rahaman, J. Mater. Sci. 39 (2004) 133—139.
[36] P.-H. Xiang, Y. Kinemuchi, K. Watari, J. Eur. Ceram. Soc. 27 (2007) 663—667.
[37] T. Kimura, T. Yamaguchi, Adv. Ceram. 21 (1987) 169.
[38] M. Ranieri, E. Aguiar, M. Cilense, A. Simões, J.A. Varela, Ceram. Int. 39 (2013) 7291—7296.
[39] Z. Zhao, X. Li, H. Ji, M. Deng, Integrated Ferroelectrics Int. J. 154 (2014) 154—158.
[40] Z. Liang, R. Huang, T. Xie, Y. Zhang, H.-T. Lin, Y. Dai, Ceram. Int. 49 (2023) 20920—20928.
[41] E.C. Aguiar, A.Z. Simões, F. Moura, M. Cilense, E. Longo, J.A. Varela, Proces. Appl. Ceram. (2011) 1—11.
[42] W. Liu, X. Wang, D. Tian, C. Xiao, Z. Wei, S. Chen, Mater. Sci. Appl. 1 (2010) 91.
[43] D. Jiang, Z. Zhou, R. Liang, X. Dong, J. Eur. Ceram. Soc. 41 (2021) 1244—1250.